Flow, Turbulence and Combustion manuscript No.
(will be inserted by the editor)

Implementation methods of wall functions in cell-vertex numerical solvers

Felix Jaegle · Olivier Cabrit · Simon Mendez · Thierry Poinsot

Received: date / Accepted: date

Abstract Two different implementation techniques of wall functions for cell-vertex based numerical methods are described and evaluated. The underlying wall model is based on the classical theory of the turbulent boundary layer. The present work focuses on the integration of this wall-model in a cell-vertex solver for large eddy simulations and its implications when applied to complex geometries, in particular domains with sudden expansions (more generally in presence of sharp edges). At corner nodes, the conjugation of law of the wall models using slip velocities on walls and of the cell-vertex approach leads to difficulties. Therefore, an alternative implementation of wall functions is introduced, which uses a no-slip condition at the wall. Evaluation is carried out on the examples of a turbulent periodic channel flow, a turbulent pipe flow with a sudden expansion to assess the performance at corners as well as an injector for aero-engines, example for an industrial-scale application with a complex geometry.

F. Jaegle
CERFACS, 42 Av. Gaspard Coriolis, 31057 Toulouse Cedex 01, France
Tel.: +33-(0)5-61 19 31 09
Fax: +33-(0)5-61 19 30 00
E-mail: felix.jaegle@cerfacs.fr

O. Cabrit
CERFACS, 42 Av. Gaspard Coriolis, 31057 Toulouse Cedex 01, France
E-mail: olivier.cabrit@cerfacs.fr

S. Mendez
CERFACS, 42 Av. Gaspard Coriolis, 31057 Toulouse Cedex 01, France
Present address: of S. Mendez
CTR, Stanford University, Bldg. 500
488 Escondido Mall, Stanford, CA 94305-3035, USA
E-mail: smendez@stanford.edu

T. Poinsot
Institut de mécanique des fluides de Toulouse (CNRS-INPT-UPS), Allée du Professeur-Camille-Soula, 31400 Toulouse, France
E-mail: thierry.poinsot@imft.fr

1 Introduction

A correct treatment of walls in Large Eddy Simulations (LES) of industrial-scale complex geometries remains a challenging task. Despite growing computing resources, mainly in the form of massively parallel machines, the resolution of boundary layer flows remains out of reach for routine application [16], making wall modeling a crucial ingredient of practical LES [11]. Alongside hybrid approaches of LES and RANS (Reynolds Averged Navier-Stokes) like Detached Eddy Simulation (DES [24, 23]), wall functions [3, 21] are often the method of choice for large LES cases (e.g. combustion chambers [20]). Here, wall functions avoid to resolve the turbulent eddies that are proportional in size to the wall-normal distance (as opposed to wall-resolved LES), as well as the strongest gradients in the viscous sublayer (which is still necessary when resolving RANS equations near the wall, as in DES approaches). The gain in terms of grid resolution is considerable [16], while very satisfying precision can be obtained even for complex flows [11].
Published studies on wall functions mainly focus on the underlying wall-model to take into account more physical details, such as heat fluxes [5], streamwise pressure gradients [7] or chemical reactions [2] just to name a few. On the other hand, relatively few sources treat the actual implementation of wall functions into a flow-solver. In this paper, it will be shown that there are several ways to couple wall functions with a numerical scheme and that these differences can affect the results of a LES. In particular, this is the case in configurations with a flow over a sudden expansion (or simply a step) and more generally in complex geometries. The study is limited to cell-vertex-type solvers. In the first part, the wall-modeling approach is laid out, followed by a description of the cell-vertex formalism, the methods of implementing wall functions therein and the related problems. Finally the different methods are evaluated and compared on several test cases ranging from a turbulent channel flow to a premixing swirler for aero-engines.

2 Wall modeling approach

Wall modeling in itself is not the main interest of the present work. Therefore, a very basic model using classical boundary layer theory is used and shall be presented briefly in the following. It should be noted that the implementation strategies presented in this paper can in principle be combined with other, more sophisticated wall law formulations. Furthermore, although turbulent heat transfer is an important part in a wall modeling approach, it shall be excluded in this paper, which will focus on momentum conservation.
The fully developed turbulent boundary layer flow over an infinite flat plate is considered. This implies that, in a Reynolds-averaged form, the problem is steady ($\partial/\partial t = 0$) and one-dimensional ($\partial/\partial x = 0$, $\partial/\partial z = 0$) with the wall-distance y being the only relevant spatial direction and the streamwise velocity $\overline{u}$ the sole non-zero mean velocity component. Here, Reynolds-averaged variables are denoted with the bar-operator $(\overline{\text{–}})$. The density ρ as well as the heat capacity at constant pressure C_P are considered constant in this context. An additional assumption is the absence of chemical reactions.

The momentum equation of the time-averaged flow then reduces to:

$$\frac{\partial \overline{p}}{\partial x} = \frac{\partial \overline{\tau_{xy}}}{\partial y} - \frac{\partial}{\partial y} \underbrace{\overline{\rho}\,\overline{u'v'}}_{\overline{\tau_t}} \tag{1}$$

Where $\tau_{xy} = \mu\ \partial u/\partial y$ is the viscous stress tensor and τ_t the Reynolds-stress tensor, which can be modeled using the Boussinesq assumption:

$$\tau_t = -\mu_t \frac{\partial \overline{u}}{\partial y} \tag{2}$$

The case of a flat plate is characterized by the absence of a longitudinal pressure gradient $\partial \overline{p}/\partial x = 0$. The momentum equation written in terms of μ and μ_t then takes the following form:

$$\frac{\partial}{\partial y}\left(\frac{\partial \overline{u}}{\partial y}\left(\overline{\mu} + \mu_t\right)\right) = 0 \tag{3}$$

This equation states that the total level of friction, $\tau_{tot} = \overline{\tau}_{xy} - \overline{\tau}_t$ is constant throughout the boundary layer. It implies that the total friction must be equal to the wall-friction, which corresponds to the viscous wall shear stress $\tau_w = \overline{\mu}\ \partial \overline{u}/\partial y|_w$, since the turbulent stress vanishes at the wall due to the absence of any fluctuations. The subscript 'w' stands for variables evaluated at the wall. Integration of equation 3 using $\tau_{tot} = \tau_w$ yields:

$$\frac{\partial \overline{u}}{\partial y}\left(\overline{\mu} + \mu_t\right) = \tau_w \tag{4}$$

For the following steps, it is convenient to introduce wall units, based on the friction velocity $u_\tau = \sqrt{\tau_w/\rho_w}$ and defined as:

$$y^+ = \frac{\rho_w u_\tau y}{\mu_w} \qquad u^+ = \frac{\overline{u}}{u_\tau} \qquad \mu^+ = \frac{\overline{\mu}}{\mu_w} \qquad \mu_t^+ = \frac{\mu_t}{\mu_w} \tag{5}$$

In wall units, the inertial layer is characterized by: $\mu_t^+ >> \mu^+$. The momentum equation 4 reduces to:

$$\frac{d\,u^+}{dy^+}\,\mu_t^+ = 1 \tag{6}$$

A closure for the turbulent viscosity, is provided by the Prandtl mixing length model [19] for an incompressible boundary layer ($\rho^+ = \overline{\rho}/\rho_w \approx 1$), which states in wall units that:

$$\mu_t^+ = (k\,y^+)^2\,\frac{du^+}{dy^+} \tag{7}$$

where k is the Von Kármán constant [9]. Injected into equation 6 and integrated, this results in the well-known logarithmic law:

$$u^+ = \frac{1}{k}\,ln(y^+) + C \tag{8}$$

The values commonly retained for the model constants are $k = 0.41$ and $C = 5.5$ for confined flows ($C = 5.2$ is rather preferred for external flows).

3 Implementation methods

3.1 The cell-vertex approach

The *cell-vertex* approach is one of the common discretization methods for finite volume schemes, the very popular alternative being the *cell-centered* formulation [6, 25]. While in the latter case, flow variables are stored at the center of the cells, they are stored at the grid nodes in the former.
The key difference is the computation of fluxes through cell boundaries. For cell-centered schemes, the flux through a cell boundary is based on the interpolation of variables situated to *either side* of the cell edge, i.e. from the *centers* of two neighbouring cells. In a cell-vertex scheme, the flux is obtained from the values at the *vertices*, i.e. at either end of the cell edge. Here, vertices are to be understood as points that coincide with the grid nodes but are associated to a grid cell. This means that one grid node can coincide with several vertices, one for each grid cell the node is connected to.

Written in flux variables, the Navier-Stokes equations take the compact form

$$\frac{\partial \mathbf{U}}{\partial t} + \vec{\bigtriangledown} \cdot \vec{\mathcal{F}} = \mathbf{S} \tag{9}$$

where $\mathbf{U}$ is the vector of the conservative flow variables, $\vec{\mathcal{F}}$ the flux tensor of $\mathbf{U}$ and $\mathbf{S}$ the vector of source terms. The flux tensor can be decomposed in a convective part $\vec{\mathcal{F}}^C$ and a viscous part $\vec{\mathcal{F}}^V$:

$$\vec{\mathcal{F}} = \vec{\mathcal{F}}^C(\mathbf{U}) + \vec{\mathcal{F}}^V(\mathbf{U}, \vec{\bigtriangledown}\,\mathbf{U}) \tag{10}$$

The first important aspect of the *cell-vertex* method is the definition of metrics, in particular of the normal vectors. Here, S_f denotes the normal vector of a given element face (or edge in 2D), defined as pointing towards the exterior. Its length is weighted by the area of the element face (resp. edge length). The normal vector $\vec{S}_k$ at the vertex k of an element (pointing inward) is obtained by

$$\vec{S}_k = \sum_{f \ni k} -\frac{d}{n_v^f} \vec{S}_f \tag{11}$$

where d is the number of spatial dimensions and n_v^f the number of vertices of face f. Figure 1 illustrates the process of calculating $\vec{S}_{k_1}$, the normal at the vertex $k = k_1$ for a triangular and a quadrilateral element. It has to be noted that this method differs for domain boundaries as explained for diffusive fluxes at the end of this section.

Based on this element description, equation 9 can be written in a semi-discretized form at node j:

$$\frac{d\mathbf{U}_j}{dt} = -\vec{\bigtriangledown} \cdot \vec{\mathcal{F}}^C\Big|_j - \vec{\bigtriangledown} \cdot \vec{\mathcal{F}}^V\Big|_j + \mathbf{S}\Big|_j \tag{12}$$

To obtain the divergence of the convective fluxes $\vec{\bigtriangledown} \cdot \vec{\mathcal{F}}^C\Big|_j$ the element residual R_e is calculated summing flux values located at all vertices k of the element e (the ensemble of these vertices being K_e):

$$\mathbf{R}_e = -\frac{1}{dV_e} \sum_{k \in K_e} \vec{\mathcal{F}}_k^C \cdot \vec{S}_k \tag{13}$$

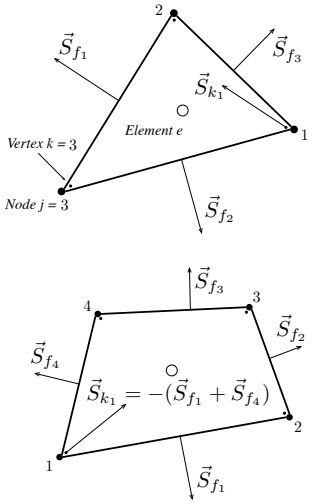

Fig. 1 Schematic of the face- (f) and vertex- (k) normals of a triangular and a quadrilateral element.

Here, V_e is the element volume which is defined as (d being the number of spatial dimensions):

$$V_e = -\frac{1}{d^2} \sum_{k \in K_e} \vec{x_k} \cdot \vec{S}_k \tag{14}$$

The nodal value of the flux divergence is then obtained by summing the weighted residuals $V_e \, \mathbf{R}_e$ of all cells having a vertex coinciding with the node j (the ensemble of these cells being noted $\mathcal{D}_j$):

$$\vec{\bigtriangledown} \cdot \vec{\mathcal{F}}^C \Big|_j = \frac{1}{dV_j} \sum_{e \in \mathcal{D}_j} \underline{\mathbf{D}}_{j,e} V_e \, \mathbf{R}_e \tag{15}$$

This summation, called *scatter*-operation, is schematized in figure 2. The nodal volume $V_j = \sum_{e \in \mathcal{D}_j} V_e / n_v^e$ is called *dual cell* as it acts as a control volume during the residual *scatter*. Here, n_v^e is the number of vertices of an element e. The residual distribution matrix $\underline{\mathbf{D}}_{j,e}$ is a central part of the numerical scheme that is built upon the cell-vertex formalism and shall not be detailed here.

For the divergence of the viscous terms $\vec{\bigtriangledown} \cdot \vec{\mathcal{F}}^V$, the method applied differs from the one used for the convective fluxes. First, the gradient of the conservative variables $\left(\vec{\bigtriangledown} \mathbf{U}\right)_e$ is calculated for the element e. Using this gradient and the nodal value $\mathbf{U}_j$ allows to calculate the viscous flux tensor from element and node values:

$$\vec{\mathcal{F}}^V_{j,e} = \vec{\mathcal{F}}^V \left((\mathbf{U})_j \, , \left(\vec{\bigtriangledown} \mathbf{U}\right)_e \right) \tag{16}$$

The divergence is then obtained by summing all contributions in the *dual cell* associated to the node j:

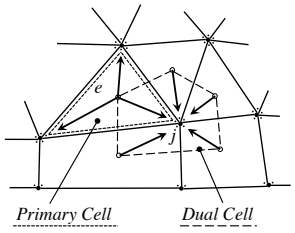

Fig. 2 Schematic of the cell-vertex formalism. The dotted line delimits an element e (primary cell), the dashed line the control volume of the node j (dual cell), arrows symbolize the scatter operation of an element residual to the surrounding nodes (equation 15).

$$\vec{\bigtriangledown} \cdot \vec{\mathcal{F}}^V \Big|_j = \frac{1}{dV_j} \sum_{e \in \mathcal{D}_j} \vec{\mathcal{F}}^V_{j,e} \cdot \vec{S}_{j,e} \tag{17}$$

The normal vectors $\vec{S}_{j,e}$ used in this operation are located at the center of a given element e and associated to the node j. Figure 3 schematizes the location and direction of these normals. It can be shown that they are equal to the vertex normals $\vec{S}_k$, where the vertex k coincides with the node j considered.

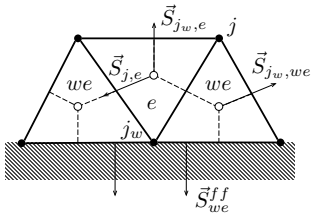

Fig. 3 Sketch of the normals $\vec{S}_{j,e}$ used for the diffusion scheme and the face-based normals $\vec{S}^{ff}_{we}$ appearing at the application of Neumann boundary conditions on elements with boundary faces, noted we.

Applying Neumann boundary conditions in a finite volume framework corresponds to imposing fluxes through the domain boundary. To do this efficiently, the diffusive flux divergence operation in equation 16 is modified for nodes located on wall boundaries, noted j_w (see figure 3): the prediction of the diffusion scheme is corrected by adding fluxes given by the boundary condition, $\vec{\mathcal{F}}^{BC}_{j_w,we}$.

$$\vec{\bigtriangledown} \cdot \vec{\mathcal{F}}^V \Big|_{j_w} = \underbrace{\frac{1}{dV_{j_w}} \sum_{e \in \mathcal{D}_{j_w}} \vec{\mathcal{F}}^V_{j_w,e} \cdot \vec{S}_{j_w,e}}_{\text{Diffusion scheme prediction}} \tag{18}$$

$$+ \underbrace{\sum_{we \in \mathcal{D}_{j_w}} \vec{\mathcal{F}}^{BC}_{j_w,we} \cdot \vec{S}^{ff}_{we}}_{\text{Boundary correction}}$$

Instead of $\vec{S}_{j,e}$, the correction term uses face-based normal vectors, noted $\vec{S}^{ff}_{we}$. They are defined as the normals of an element face located on the boundary, as shown in figure 3 for the boundary elements (denoted by we).

3.2 The use of wall functions in LES solvers

In sections 2 and 3.1, the wall model and the numerical framework have been described. The missing ingredient for the implementation of wall laws is how numerics and wall model are combined *in a LES context*. For the sake of clarity, the following paragraphs are limited to a one-dimensional view (in wall-normal direction), analogous to turbulent boundary layer theory. The shear balance in the element adjacent to the wall (noted 'we') takes the form:

$$\tau_{xy}\Big|_{we} = \frac{d\,\hat{u}}{dy}\Big|_{we} (\mu\,|_{we} + \mu_{sgs}|_{we}) = \frac{\hat{u}_2 - \hat{u}_1}{\Delta y} (\mu\,|_{we} + \mu_{sgs}|_{we}) \tag{19}$$

where u_1 and u_2 are the velocities at directly on the wall and on the first grid point respectively, '$\hat{}$' is the LES filter operator, Δy is the wall-distance of the first point and μ_{sgs} the subgrid-scale viscosity. In cases of low near-wall grid resolution, this equation cannot yield correct results: the subgrid-scale viscosity is given by a LES model that is designed to account for stresses in the unresolved scales of turbulence. Near the wall, however, typical models will fail to predict the wall shear stress correctly, as they are not based on physical arguments related to under-resolved, wall-bounded flows. Instead, their behaviour is known to be often unphysical in under-resolved boundary-layers or generally in zones of pure shear [13], for instance in the case of the Smagorinsky model [22].

The central idea of wall functions consists in locally using boundary layer theory (of the type layed out in section 2) in lieu of the diffusion scheme to restore the correct balance in equation 19. In the element adjacent to the wall, the predicted shear stress $\tau_{xy}|_{we}$ is corrected by a value obtained from a wall model, $\overline{\tau}_w^{model}$.

$$\tau_{xy}\Big|_{we} = \overline{\tau}_w^{model} \tag{20}$$

In the present study, $\overline{\tau}_w^{model}$ is obtained from the logarithmic law (equation 8). Written in flow variables, it reveals its practical property of relating the wall shear stress to any point in the velocity profile located inside the inertial layer:

$$\hat{u} = \frac{1}{k}\sqrt{\frac{\overline{\tau}_w}{\rho_{we}}}\, ln\left(\frac{\rho_w y \sqrt{\overline{\tau}_w/\rho_{we}}}{\mu|_{we}}\right) + C \tag{21}$$

In practice, this equation can be numerically resolved to provide the wall shear stress as a function of the velocity $\hat{u}_2$ at the first off-wall point with the wall distance Δy (assuming ρ_{we} and μ_{we} to be constant):

$$\overline{\tau}_w = f(\Delta y, \hat{u}_2) \tag{22}$$

Note that this approach involves Reynolds-averaged variables (noted with the bar operator ‘ $-$ ’) as filtered variables of the LES. In a wall function approach, it is generally assumed that the near-wall control volume contains a sufficient number of turbulent structures for a Reynolds averaged view to be justified, even in an instantaneous flow field [16]. RANS quantities in the first cell can therefore be combined with instantaneous variables of the LES.

The following sections describe in detail different options of applying equation 21 to the numerical scheme as a wall boundary condition.

3.3 Implementation with slip velocity at the wall

The first, classical method to implement wall functions starts from the idea that corrections should be limited to the nodes on the domain boundary. This can be considered an advantage on unstructured triangle- or tetraedra meshes, where element type and topology are of little influence. In view of the cell-vertex formalism, this means that the predictions of the diffusion scheme have to be modified when summing the contributions of the viscous fluxes at the dual cell associated to each boundary node (eq. 17). This procedure, illustrated in figure 4, consists in having the scheme calculate the wall-normal momentum flux τ_{xy} and subsequently replacing the contributions headed to the wall nodes by the value corrected with the wall function τ_{we}. In an arbitrary 3D geometry, this correction is applied selectively on the wall-normal component of the momentum flux, the direction of shear being aligned with the wall-parallel velocity vector. Finally, the wall-normal velocity is set to zero ($u_{1,\perp} = 0$) as a Dirichlet-type boundary condition (classical Dirichlet or the NSCBC (for Navier Stokes Characteristic Boundary Conditions) [18] equivalent). As nothing is imposed for the wall-parallel velocity, a non-negligible slip-velocity appears on the wall as the scheme advances in time. This velocity has no physical meaning: it should be regarded as a free parameter in the computation as its value depends predominantly on the level of subgrid-scale viscosity in the wall element. This becomes clear when rearranging equation 19 at the wall-element with $\overline{\tau}_w$ obtained from the wall function.

$$\left.\frac{d\,\hat{u}}{dy}\right|_{we} = \frac{\overline{\tau}_w(\hat{u}_2, y_2)}{\mu\,|_{we} + \mu_{sgs}|_{we}} \tag{23}$$

Assuming that the velocity at the first node above the wall behaves ideally and thus coincides with the log-law for a given $\overline{\tau}_w$ and the molecular viscosity μ is constant, this equation yields a gradient that will establish between y_1 and y_2, which depends only on μ_{sgs} (see figure 5 for an illlustration). This relation reveals that the method is well-suited for the use in conjunction with the Smagorinsky model, which provides for (unphysically) high levels of subgrid-scale viscosity near the wall, leading to a moderate gradient. In contrast, when used with turbulence models that yield near-zero subgrid-scale velocity at the wall (e.g. WALE [13]), this gradient will be very steep and can lead to reversed slip-velocities, causing spurious oscillations.
For the Smagorinsky model, one can further estimate the magnitude of the slip-velocity

obtained on the wall by writing it in a time-averaged ($\langle\rangle$-operator), one-dimensional form (assuming a linear discretization of the velocity profile):

$$\langle \mu_{sgs}|_{we} \rangle = \langle \rho_{we} \rangle \left(C_s \Delta\right)^2 \frac{\left(\langle \hat{u}_2 \rangle - \langle \hat{u}_1 \rangle\right)}{y_2} \tag{24}$$

Here, C_s is the Smagorinsky constant and Δ a length scale for the cell size. The slip-velocity can be estimated as:

$$\langle \hat{u}_1 \rangle = \langle \hat{u}_2 \rangle - y_2 \frac{\langle \overline{\tau}_w \rangle}{\langle \mu\,|_{we} \rangle + \langle \mu_{sgs}|_{we} \rangle} \tag{25}$$

Combining equations 24 and 25 finally allows to obtain the average slip velocity $\langle \hat{u}_1 \rangle$ explicitely:

$$\langle \hat{u}_1 \rangle = \langle \hat{u}_2 \rangle - \frac{y_2}{2\,\langle \rho_{we} \rangle (C_s \Delta)^2} \left(-\langle \mu|_{we} \rangle + \sqrt{\langle \mu\,|_{we} \rangle^2 + 4 \langle \rho_{we} \rangle^2 (C_s \Delta)^2 \langle \overline{\tau}_w \rangle} \right) \tag{26}$$

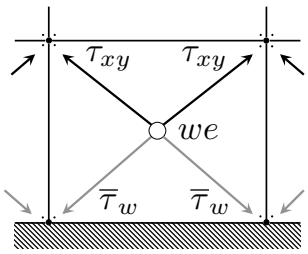

Fig. 4 Application of the wall functions in the slip-wall formulation. Schematic of the *scatter* operation of the momentum flux contributions. Black arrows correspond to contributions calculated by the diffusion scheme, grey arrows to contributions corrected by the wall function.

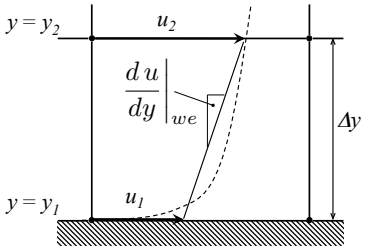

Fig. 5 Overview of the most important variables appearing in the formulation with a slip velocity.

3.4 Corner problem with slip velocity at walls

The procedure, described in section 3.3 leads to a difficulty at corner points. Unlike the Neumann boundary conditions that are applied on the boundary face (see equation 18), the Dirichlet conditions of zero wall-normal velocity are applied directly on the conservative variables at the nodes. At the node coinciding with the corner, the definition of the wall-normal vectors is ambiguous (see figure 6). Following the standard procedure of calculating the nodal wall normal $\vec{S}_j^b$ as the average of the surrounding boundary-face normals $\vec{S}_e^{ff}$, the resulting normal at the corner point $\vec{S}_{j,c}^b$ (and consequently also the velocity vector) would take an unphysical angle of ≈ 45 degrees. Therefore, at the corner point only, the normal is either chosen equal to the one of the upstream boundary face or set to zero (removing all constraints on the direction of the velocity). Both methods lead to a nodal velocity vector that is aligned with the upstream wall. As a result, however, mass conservation will no longer be respected because of a flux through the boundary face situated at the downstream wall, as illustrated in figure 7.1. To correct that, a (face-based) Neumann boundary condition of zero mass flux can be applied instead of the Dirichlet condition of zero normal velocity. This ensures mass conservation but the correction of the face downstream of the corner effectively reduces the slip-velocity at the corner, leading to perturbations of the flow-field in this area. As the wall-element in a mesh adapted for wall functions is of a relatively large size in order to reach into the inertial layer, these perturbations can take magnitudes that lead to unphysical flow fields or numerical instabilities (see section 4.2).

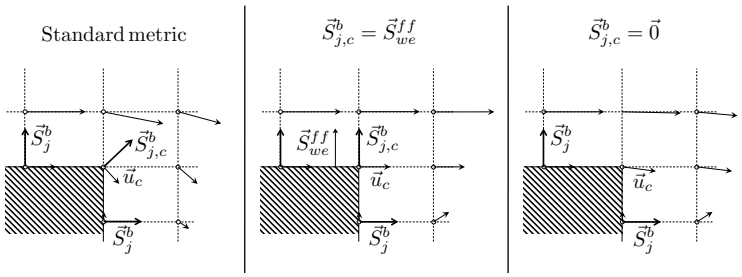

Fig. 6 Schematic illustration of different definitions of the nodal normal vector $\vec{S}_{j,c}$ at the corner node. Generic configuration of a flow over a corner.

Note that these difficulties are limited to the cell-vertex approach, as illustrated in figure 7: for a cell-centered formulation (figure 7.3), the wall-normal vector ambiguities and problems of mass-conservation do not appear due to the location of the velocity vectors at the cell-center. In a cell-vertex formalism, these problems can easily be overcome if a no-slip condition is imposed at the wall nodes as shown in figure 7.2. The following sections are therefore dedicated to wall functions with a no-slip condition at the wall.

3.5 Implementation without slip velocity at the wall

The need for an alternative implementation method of wall functions in cell-vertex solvers arises from the problems listed in section 3.4. The idea is consequently to

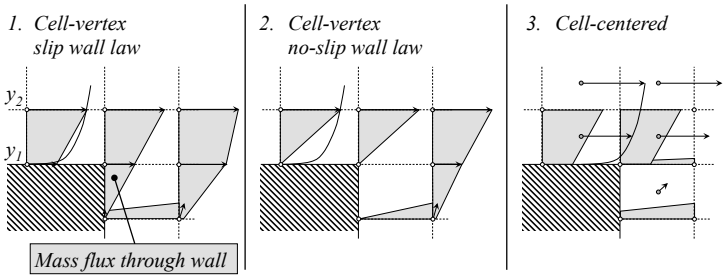

Fig. 7 Schematic of mass fluxes in vicinity of a corner ('→' symbolizes a momentum vector), comparing a cell-vertex scheme with/without slip velocity to the cell-centered approach. Generic configuration of a flow over a corner.

impose a no-slip condition on the wall nodes, which, however, prohibits the application of the wall shear stress at the same location. This is because, in a given timestep, the corrected contributions of the diffusion scheme τ_{we} exclusively affect the nodes they are directed to. Neighbouring nodes are only influenced indirectly in subsequent timesteps. A Dirichlet-condition, imposed after the computation of the diffusive terms will therefore cancel out any effect of the numerical scheme on these nodes. The logical alternative is to apply the wall function away from the wall, at the upper nodes of the first cell, as shown in figure 8. This choice is in fact consistent with the underlying boundary layer theory, as equation 3 clearly shows that the shear is constant throughout the first wall cell (equal to τ_w). The fact that the gradient inside the wall element (figure 9) is unphysically high has no consequence in this case, because the diffusion scheme is completely inactive in this cell, its predictions being entirely replaced by the wall function and the no-slip condition.

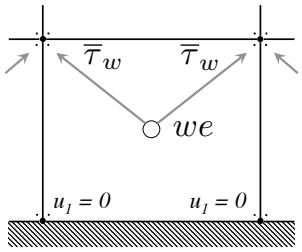

Fig. 8 Application of the wall functions in the no-slip formulation. Schematic of the *scatter* operation of the momentum flux contributions. Grey arrows symbolize the contributions corrected by the wall function.

An overview of the key differences between both implementation methods can be obtained from table 1, where a simplified sequence of events during a numerical timestep is presented.

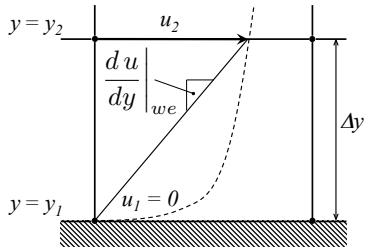

Fig. 9 Overview of the most important variables appearing in the no-slip formulation.

3.6 Limitations of the no-slip approach

The no-slip formulation removes all difficulties related to domains with corners. However, it is compatible only with certain element types at the wall. The slip-wall formulation can be deployed on any type of mesh, as it is an approach limited to the boundary of the domain. The no-slip approach, as it acts inside the fluid *volume*, cannot sensibly be implemented for arbitrary element types. The key example is a pure tetraedra mesh, where the algorithms to establish the connectivity to the off-wall vertices (where the wall function would be applied) are complex and costly. Furthermore, the irregular wall-distances have lead to oscillatory behaviour in the tests that were conducted. The no-slip approach is therefore limited to all sorts of prismatic elements (typically prisms and hexaedra) that ensure uniform wall-distance and straightforward access (in terms of connectivity) to the 'upper' element vertices. The capability of treating hybrid, unstructured meshes is therefore a prerequisite for the use of no-slip wall functions in complex geometries. This is not a very strong limitation as the use of prismatic elements near the wall can generally be expected to lead to better results than a purely tetraedral mesh.

4 Applications and Results

In the following, both implementation methods are applied to three different cases with increasing complexity. Each application, together with a discussion of the results is presented in an individual section.

4.1 Turbulent channel flow

A Large Eddy Simulation of a periodic channel flow serves as a first test case for the validation of both wall function implementations on smooth walls without corners. The configuration consists of a doubly periodic box (in x- and z direction) with walls on the top and bottom surfaces (in y-direction). Six different cases are considered (a summary is given in table 2), distinguished by different Reynolds number, based on bulk properties (subscript 'b'), defined as:

No-slip wall law	**Slip wall law**
Initial field of conservative variables $\mathbf{U}$	
Calculation of the flux tensor $\vec{\mathcal{F}}$	
Neumann boundary conditions	
τ_w at y_2 (1st off-wall node)	τ_w at y_1 (wall)
Advancement in time: $\partial\mathbf{U}/\partial t + \vec{\nabla} \cdot \vec{\mathcal{F}} = \mathbf{S}$	
New field of conservative variables $\mathbf{U}$	
Correction of conservative variables $\mathbf{U}$ Dirichlet boundary conditions	
$u_1 = 0$	$u_{1,\perp} = 0$
Final field of conservative variables $\mathbf{U}$	

Table 1 Comparative overview of the no-slip and slip wall function implementations. Simplified sequence of events during one computational time step.

#	Re_b	Re_τ	y^+	grid nodes	$2\,\delta$ $[m]$
1	20 000	≈ 322	≈ 30	29 x 21 x 29	$1.5\ 10^{-3}$
2	40 000	≈ 594	≈ 50	33 x 25 x 33	$3.0\ 10^{-3}$
3	80 000	≈ 1100	≈ 100	25 x 23 x 25	$6.0\ 10^{-3}$
4	200 000	≈ 2524	≈ 100	33 x 51 x 33	$1.5\ 10^{-2}$
5	400 000	≈ 4798	≈ 150	33 x 61 x 33	$3.0\ 10^{-2}$
6	2 000 0000	≈ 20816	≈ 1000	41 x 41 x 41	$1.5\ 10^{-1}$

Table 2 Summary of the turbulent periodic channel cases.

$$Re_b = \frac{\rho_b D_h\, u_b}{\mu_b} \tag{27}$$

Where $D_h = 4\delta$ is the hydraulic diameter. The mesh in all cases is of uniform, cartesian type with grid resolutions adapted to the respective values of Re_b. All results are obtained using the second-order accurate Lax-Wendroff scheme [12].

Detailed statistics are presented in figures 10 and 11 for a single, typical case (# 4) at $Re_b = 200\,000$, which corresponds to a friction Reynolds number of $Re_\tau \approx 2524$. Figure 10 shows profiles of dimensionless longitudinal velocity u^+. There is a good agreement between the logarithmic law, DNS data of Hoyas and Jiménez [8] and both LES simulation results near the first grid point, showing that the most direct effect that wall functions have on the flow is correctly reproduced. In the region of the first few grid points towards the center of the channel, profiles from both wall functions start to deviate from the logarithmic law, an effect that is slightly stronger in the no-slip formulation. This is most probably due to under-resolved and thus unphysical turbulent mechanisms near the wall, which are a result of the inherent lack of grid resolution that is described, for instance, by Nicoud et al. [14] (in the context of a wall function approach) and studied in a more general context by Piomelli et al. [17].

In this intermediate layer, the subgrid-scale viscosity is given by a LES model and therefore takes values that are lower than a turbulence model in a RANS approach would predict, leaving a share of the stress balance to be accounted for by resolved Reynolds stresses. On the other hand, the grid resolution in these zones is determined by the wall function approach and therefore too coarse to resolve turbulent structures at scales small enough for a LES to result in correct Reynolds stresses. A study of the resolution requirements in LES of shear flows can be found in the work of Baggett et al. [1]. Differences between both formulations can be observed on the velocity fluctuation

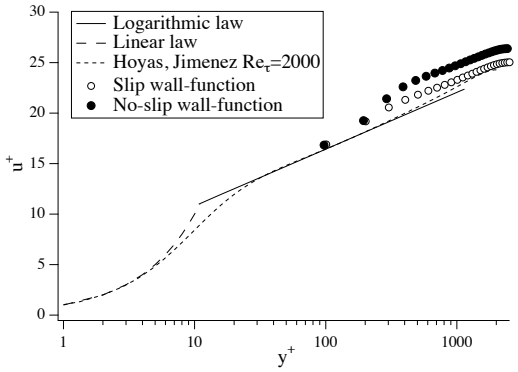

Fig. 10 Turbulent channel, dimensionless velocity profiles. Comparison between the analytical profile, DNS data [8] and LES results, obtained with a second-order Lax-Wendroff scheme, using wall functions in slip- and no-slip formulation. Case of $Re_b = 200000$.

profiles shown in figure 11 where the peak of the no-slip wall functions is displaced by approximately one point away from the wall with respect to the one of the slip-wall function. This indicates that for the slip-formulation the under-resolved near-wall vortical structures can be accomodated by the wall nodes thanks to the presence of a slip velocity, whereas in the case of the no-slip results, these structures are shifted away from the wall (figure 12), which seems to slightly increase their negative effect.

An overview of the global performance of both wall functions over a wide range of Reynolds numbers is shown in figure 13. Here, the mean friction coefficient C_f of the channel flow is compared to the classical correlations of Kármán and Nikuradse [10] as well as Petukhov [15]. The general trend observed is that for low Reynolds numbers, the slip-formulation yields superior results but deteriorates slightly for increasing Re_b. Inversely, the no-slip formulation shows the largest errors for low Reynolds numbers with increasingly good agreement for growing Re_b, eventually surpassing the accuracy of the slip-formulation. This observation can be explained by the diminishing influence of the near-wall effects relative to the channel height that work to the disadvantage of the no-slip formulation.

4.2 Flow over a sudden expansion

The flow over a sudden expansion is well-suited as a test case for the corner problem. It consists of a circular upstream tube of diameter D from which the flow enters a larger

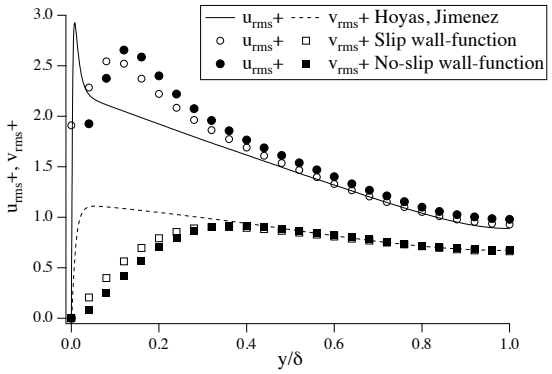

Fig. 11 Turbulent channel, dimensionless velocity fluctuation profiles. Comparison between the analytical profile, DNS data [8] and LES results, obtained with a second-order Lax-Wendroff scheme, using wall functions in slip- and no-slip formulation. Case of $Re_b = 200000$.

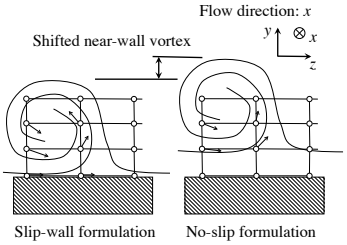

Fig. 12 Sketch of the effect of shifted near-wall vortical structures comparing slip- and no-slip formulations.

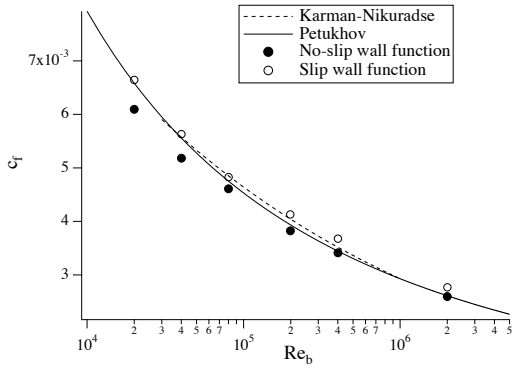

Fig. 13 Wall friction coefficient C_f as a function of the Reynolds number Re_b based on the bulk velocity in the channel. Comparison of slip- and no-slip results with correlations of Kármán and Nikuradse [10] as well as Petukhov [15].

tube of diameter $2\,D$ (see figure 14). This corresponds to the experiment of Dellenback et al. [4] from which experimental data is available. The mesh is composed entirely of hexaedral elements with 10 cells across the diameter of the upstream tube, which

results in a first off-wall grid point situated at approximately 160 wall units. The mean velocity profile from experimental data is imposed at the inlet. The resulting flow has a Reynolds number of 30 000 and transitions naturally to a turbulent state after the step. The degree of physical detail in this simulation is clearly insufficient for an accurate representation of the flow phenomenon at hand, but in this case, this is not the intent. Instead, this geometry, in conjunction with the very coarse grid resolution, is typical of certain geometrical details in very large LES cases, which often include small-scale jets that are emitted by tubes or conduits into a larger reservoir. Examples are dilution holes in combustion chambers or the narrow passage around the valves of an internal combustion engine, which are often meshed quite coarsely. It is typically in this kind of configuration that the corner problem leads to undesired modifications of the flow field or to numerical artefacts.

Qualitative differences between the wall-law formulation can be observed on the iso-contours of mean axial velocity shown in figure 15. The flow field remains totally unaffected (figure 15, top) for slip wall functions in their non-conservative form, i.e. without correction of wall-normal mass flux (see section 3.4, figure 7). Note that the absence of this correction leads to an unphysical mass flux through the wall downstream of the step that amounts to approx. 15 % of the global mass flux. On the other hand, a clear distortion at the height of the step can be observed when the mass-flux correction is applied. This correction reduces the slip velocity at the corner points and leads to an unphysical acceleration of the flow in the center (figure 15, center). Furthermore, this very localized modification of the flow field causes numerical point-to point oscillations. The said distortion is not observed for wall functions in the no-slip formulation (figure 15, bottom). A more quantitative view of the problem is presented in figure 16, which shows the normalized, mean axial velocity on the centerline in direct vicinity of the step ($x = -0.5\,D$ to $x = D$) compared to experimental data [4]. As the flow is virtually incompressible, one would expect the centerline velocity to remain constant in this area, which is confirmed by the experiment. The simulation results of the slip wall function, however, show a clearly unphysical acceleration. The result using no-slip wall functions is a clear improvement as the centerline velocity remains globally constant despite a slightly oscillatory behavior at the coordinate of the step.

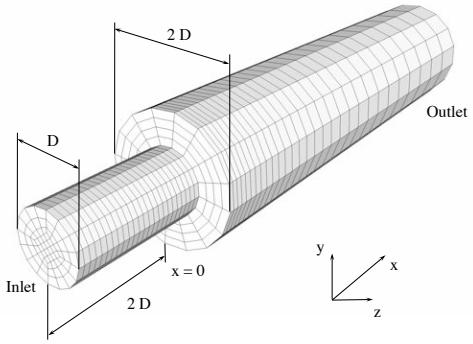

Fig. 14 Flow over a sudden expansion: Mesh and geometry overview.

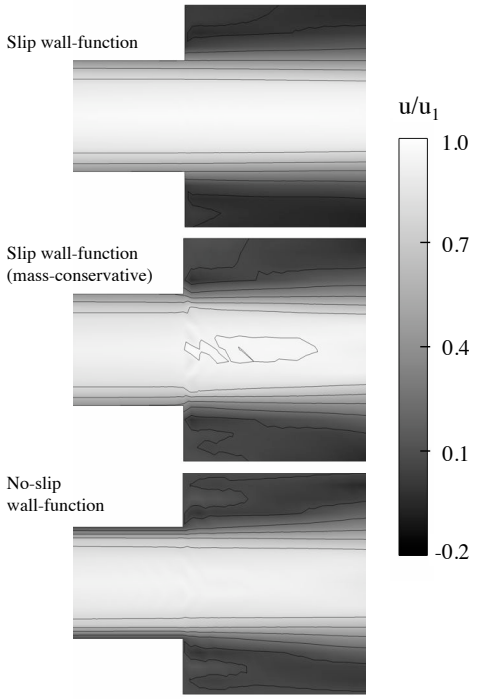

Fig. 15 Mean axial velocity iso-contours of the flow over a sudden expansion. Top: slip wall function without correction (not mass-conservative). Center: slip wall function with correction. Bottom: no-slip wall function.

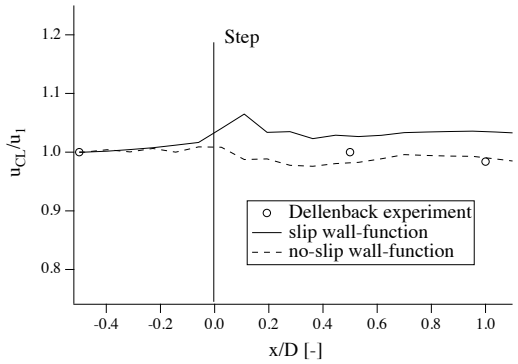

Fig. 16 Flow over a sudden expansion: Ratio of centerline velocities u_{CL} and the centerline velocity at $x = -0.5\,D$, u_1, for slip- and no-slip wall functions compared to experimental data (Dellenback et al. [4]). The diagram shows time-averaged results.

4.3 Injector for aero-engines

The last application is an academical combustion chamber with one single premixing swirler like it is typically found in the latest generation of aero-engine combustors

(figure 17). It is an example for one of the more complex geometries encountered in LES. The swirler is characterized by three stages, each composed of a series of narrow channels separated by the guide vanes, as highlighted in the right part of figure 17. Here, it is operated in a purely aerodynamic regime (without liquid fuel injection or combustion) in order to assess the capability of the novel wall-model implementation. The chamber is pressurized at 4.3 bar, the air fed into the plenum is pre-heated to 473 K, which corresponds roughly to the operating conditions of an engine at partial load. The airflow from the plenum to the chamber is split between the three-staged swirler and a cooling film placed near the circumference of the chamber upstream wall. Owing to the complexity of the computational domain, the grid is composed of tetraedral elements in its volume and of one single layer of prismatic elements at the boundary where wall functions are applied (see section 3.6 for details on the necessity of this method). This approach is applicable in arbitrary geometries as it simply consists in extruding the triangular tesselation of the domain boundary towards the inside. However, the more prismatic layers one chooses to apply or the thicker the layers are, the more the prisms tend to be distorted on sharp edges or corners. A view of the mesh and a detail of the prismatic layer is shown in figure 18. The thickness of the prism layer is varied locally and carefully adapted to be as close as possible to 100 wall units. The resulting mesh comprises approximately 8.5 million cells and 1.6 million nodes. The simulations were performed using the second-order accurate Lax-Wendroff scheme [12]. In the two simulations compared below, the only difference is the wall treatment. Everything else remains the same (mesh, algorithms, timestep).

Fig. 17 Left: cut-away view of the injector. Right: transparent view with swirler stages highlighted.

Quantitative results are presented in the form of mean velocity profiles (figure 20) and RMS velocity profiles (figure 21). In both figures, the axial and tangential components obtained with both wall function formulations are compared to experimental data provided by ONERA Fauga-Mauzac. The profiles are extracted over three transverse lines positionned at 10, 15 and 30 mm downstream of the swirler exit (see figure 19). The agreement of the no-slip results in axial direction with experimental data is excellent, both the position and the magnitude of the peaks corresponding to the central flow and the cooling films are accurately reproduced. This is observed on all three measurement positions. The results of the slip wall functions are less satisfying because the peaks of the main flow are shifted slightly towards the center, indicating that the opening angle of the cone-shaped flow is too small. Purely qualitatively, this discrepancy in opening angle can also be observed on the instantaneous velocity field, shown in figure 19. As a consequence, the peak magnitudes increase, a behavior that

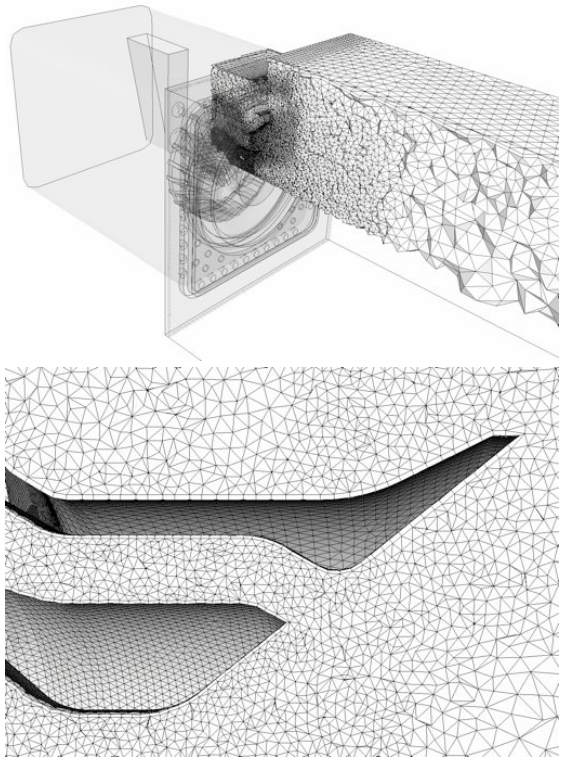

Fig. 18 Mesh overview and detail of hybrid wall boundary region with a layer of prismatic elements.

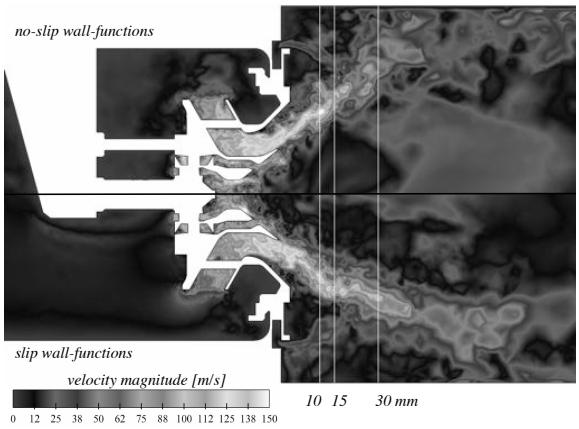

Fig. 19 Instantaneous velocity magnitude contours on a central cross-section through the domain. Upper half: result obtained using no-slip wall functions. Lower half: result obtained using slip wall function. White lines: positions of the extraction of velocity profiles.

is observed consistently at all three positions. In the tangential direction, the same observations can be made: very good agreement for the no-slip formulation and an over-estimation of tangential velocity peaks due to a under-estimated opening of the main flow.

Differences are less pronounced for the axial velocity fluctuations shown in figure 21.

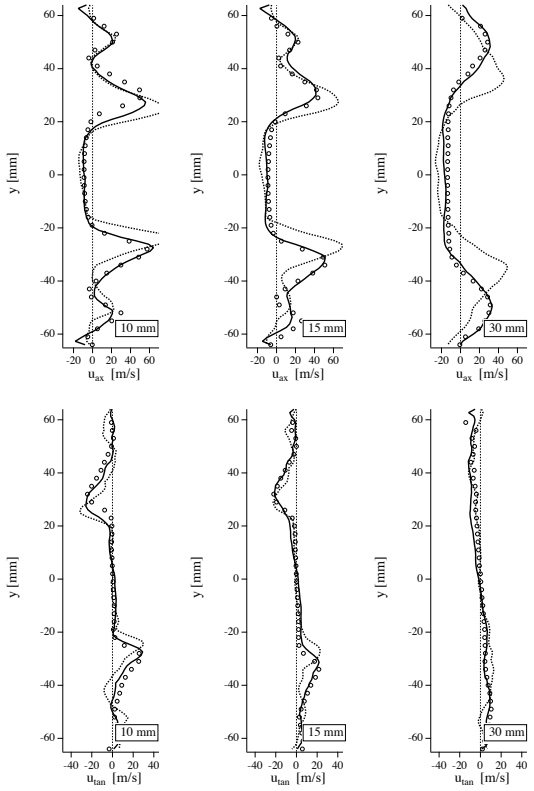

Fig. 20 Mean velocity profiles. Axial component (upper diagram) and tangential component (lower diagram). Comparison of no-slip wall functions (—), slip wall functions (- - -) and experimental data (○ ○ ○).

Here, the magnitude of the strongest fluctuations in the turbulent shear layer between the main flow and the central recirculation zone is well captured in both simulations. Differences are observed on the third measurement line at 30 mm, where the offset of the peaks from the slip wall function results becomes most noticeable. In tangential direction, fluctuations are slightly over-estimated on the first measurement line (10 mm) in both simulations. Downstream, the agreement is better for the no-slip results, while the slip wall functions again show over-estimated peaks displaced towards the inside.

The quality of both LES (without considering the differences resulting from wall modeling) is very satisfying as shown by the results obtained using the no-slip wall function approach. With all other simulation parameters (mesh, numerical scheme, turbulence model etc.) being identical, the discrepancies observed relative to the slip wall function

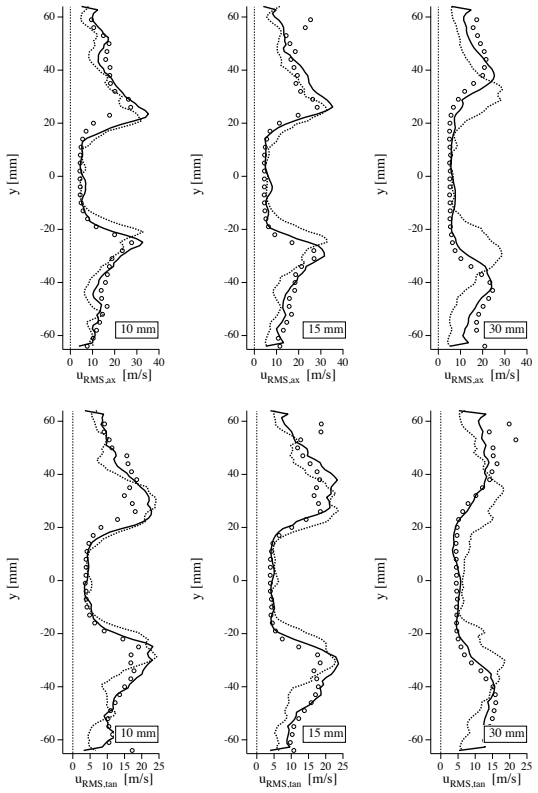

Fig. 21 Velocity fluctuation profiles. Axial component (upper diagram) and tangential component (lower diagram). Comparison of no-slip wall functions (—), slip wall functions (- - -) and experimental data (○ ○ ○).

formulation show that the *implementation* of the wall model alone can lead to significantly different results in a realistic application. Here, the reason for the differences is not attributed to the corner problem described in sections 3.4 and 4.2 but to the tendency of the slip velocity (which forces the near-wall momentum in wall-parallel direction) to keep the flow closely attached to curved geometrical features. In this case, the main flow concentrates along the shape of the inner lip of the injector cone, which results in a more confined shape of the overall flow.

Note that the favourable behaviour of the no-slip formulation should not be confounded with the capability to predict boundary layer detachment, which remains out of reach for a wall-model that neglects the streamwise pressure gradient. However, even with a suitable underlying wall-model, the slip-wall formulation still cannot be expected to predict detachment correctly. This is because the near-wall momentum is transported to a non-negligible extent by the slip velocity, which is necessarily aligned with the wall and in its magnitude depends mainly on the level of subgrid scale viscolity μ_{sgs}, as highlighted by equations 25 and 26. This means that the onset of the detachment (a vanishing slip-velocity) would be piloted by the LES subgrid-scale turbulence model – a clearly non-physical mechanism.

Another important aspect is the numerical robustness of either approach. An instruc-

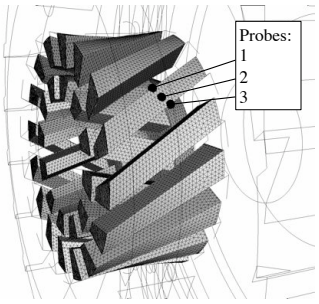

Fig. 22 Location of the pressure probes. View of the two innermost swirler stages.

tive way of looking at this issue is to observe the temporal evolution of pressure and slip velocity at a set of probes located on the wall of a narrow channel. The arrangement of the three probes considered is shown in figure 22. The evolution of the slip velocity x-component, presented in figure 23 reveals its very unstable behavior. While it is observed in the turbulent channel flow that the slip-velocity accommodates to the natural near-wall fluctuations to a certain extent (see fig. 11), it becomes clear that in the case of a less resolved and less regular mesh, the slip-velocity reveals a non-physical strong oscillatory tendency up to the point of briefly taking counterstreamwise orientations. The resulting pressure fluctuations are five times stronger than in the case of the no-slip formulation, as shown in figure 24. Obviously, this would become an issue if the LES was used for aeroacoustics simulations, where wall functions in slip-formulation create a non-physical noise. Furthermore, the advantages of the no-slip formulation in terms of a problem-free (i.e. more robust at locations that are prone to destabilizing the numerics) application by the end-user and the gained rapidity in setting up a simulation should not be under-estimated.

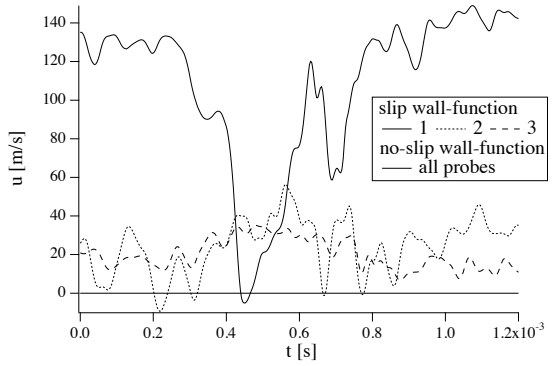

Fig. 23 x-component of the velocity recorded at the three probes over a period of 1.2 milliseconds. Comparison of results from slip- and no-slip wall functions.

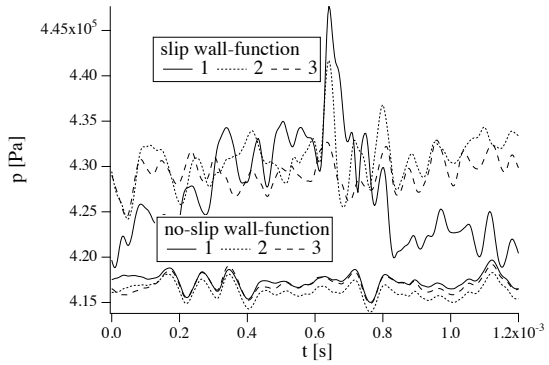

Fig. 24 Pressure signal recorded at the three probes over a period of 1.2 milliseconds. Comparison of results from slip- and no-slip wall functions.

5 Conclusion

Two different implementation methods of wall functions in cell-vertex type solvers have been laid out. The classical method imposes the shear-stress from the wall model directly at the boundary, which results in a slip-velocity at the wall itself. The artificial nature of this slip-velocity and its negative consequences on certain configurations encountered in real-world LES applications has been highlighted. To avoid these difficulties, a formulation with a no-slip condition at the wall is proposed. The wall shear-stress is applied at the first off-wall node, which leads to the necessity of using hexaedral or prismatic meshes in near-wall regions.

Both formulations are compared in three different test cases. The first is the turbulent, periodic channel flow, which allows to verify the capability of both approaches to reproduce the quantities given by theory and DNS data. The second is the flow over a sudden expansion, which reveals the problems created by the slip wall functions at corner points and shows that the no-slip formulation is not affected. The third case is an injector for aero-engines that is typical of complex geometries in realistic applications.

It is shown that the proposed no-slip formulation has superior qualities in reproducing the experimental velocity profiles, which is explained by the increased tendency of the slip wall functions to force the flow into wall-parallel direction along curved surfaces, resulting in a slightly altered flow topology. Furthermore, the tendency to oscillatory behaviour of the slip-velocity in certain cases and its impact on numerical robustness is highlighted.

It can be stated that in realistic applications, the way a wall-model is implemented in a given code and the way it interacts with the numerical methods used (in particular: scheme and SGS turbulence model) *can* influence the results as much as the wall-model itself. While the present work uses a very basic model, the performance of the proposed no-slip formulation in conjunction with more sophisticated models should be further investigated.

Acknowledgements The authors greatly acknowledge the support of ONERA Fauga-Mauzac center in providing measurement data. The support of F. Jaegle by the European community through a Marie Curie Fellowship (contract MEST-CT-2005-020426) is gratefully acknowledged.

References

1. Baggett JS, Jimenez J, Kravchenko AG (1997) Resolution requirements in large-eddy simulations of shear flows. Center for Turbulence Research Annual Research Briefs pp 51–66
2. Cabrit O, Nicoud F (2009) Direct simulations for wall modeling of multicomponent reacting compressible turbulent flows. Phys. Fluids 21(055108)
3. Deardorff J (1970) A numerical study of three-dimensional turbulent channel flow at large reynolds numbers. J. Fluid Mech. 41:453–480
4. Dellenback P, Metzger D, Neitzel G (1988) Measurement in turbulent swirling flows through an abrupt axisymmetric expansion. AIAA J. 13(4):669–681
5. Grötzbach (1987) Direct numerical and large eddy simulation of turbulent channel flows. In: Cheremisinoff NP (ed) Encyclopedia of Fluid Mechanics, Gulf, West Orange, NJ, pp 1337–1391
6. Hirsch C (1988) Numerical Computation of internal and external flows. John Wiley, New York
7. Hoffmann G, Benocci C (1995) Approximate wall boundary conditions for large eddy simulations. In: R B (ed) Advances in turbulence V, Kluwer Academic Publishers, pp 222–228
8. Hoyas S, Jiménez J (2006) Scaling of the velocity fluctuations in turbulent channels up to re= 2003. Phys. Fluids 18:011,702
9. von Kármán T (1930) Mechanische aehnlichkeit und turbulenz. Nach Ges Wiss Göttingen, Math Phys Klasse 1:58–76
10. Kays W, Crawford M, Weigand B (2004) Convective heat and mass transfer. McGraw-Hill Science/Engineering/Math
11. Mohammadi B, Puigt G (2006) Wall functions in computational fluid mechanics. Comput. Fluids 35(10):1108–1115
12. Ni RH (1982) A multiple grid scheme for solving the euler equations. AIAA J. 20:1565–1571
13. Nicoud F, Ducros F (1999) Subgrid-scale stress modelling based on the square of the velocity gradient. Flow Turb. and Combustion 62(3):183–200
14. Nicoud F, Baggett J, Moin P, Cabot W (2001) Les wall-modeling based on optimal control theory. Phys. Fluids 13(10):1629–1632
15. Petukhov B (1970) Heat transfer and friction in turbulent pipe flow with variable physical properties. Advances in heat transfer 6:503–564
16. Piomelli U, Balaras E (2002) Wall-layer models for large-eddy simulations. Ann. Rev. Fluid Mech. 34(1):349–374
17. Piomelli U, Balaras E, Pasinato H, Squires K, Spalart P (2003) The inner–outer layer interface in large-eddy simulations with wall-layer models. Int. J. Heat Fluid Flow 24(4):538–550
18. Poinsot T, Lele S (1992) Boundary conditions for direct simulations of compressible viscous flows. J. Comput. Phys. 101(1):104–129
19. Prandtl L (1925) Bericht über untersuchungen zur ausgebildeten turbulenz. Zeitschrift fur angewandte Mathematik und Mechanik 5:136 – 139

20. Schmitt P, Poinsot T, Schuermans B, Geigle K (2007) Large-eddy simulation and experimental study of heat transfer, nitric oxide emissions and combustion instability in a swirled turbulent high pressure burner. J. Fluid Mech. 570:17–46
21. Schumann U (1975) Subgrid scale model for finite difference simulations of turbulent flows in plane channels and annuli. J. Comput. Phys. 18:376–404
22. Smagorinsky J (1963) General circulation experiments with the primitive equations: 1. the basic experiment. Monthly Weather Review 91:99–164
23. Spalart P (2009) Detached-eddy simulation. Ann. Rev. Fluid Mech. 41:181–202
24. Spalart P, Jou W, Strelets M, Allmaras S (1997) Comments on the feasibility of LES for wings, and on a hybrid RANS/LES approach. Advances in DNS/LES 1
25. Tannehill J, Anderson D, Pletcher R (1997) Computational fluid mechanics and heat transfer. Hemisphere Publishing Corporation